Intracellular dynamics of hippocampal place cells during virtual navigation

Christopher D. Harvey[1,2], **Forrest Collman**[1,2], **Daniel A. Dombeck**[1,2], and **David W. Tank**[1,2]

[1] Princeton Neuroscience Institute

[2] Dept. of Molecular Biology, Princeton University, Princeton, NJ 08544

Abstract

Hippocampal place cells encode spatial information in rate and temporal codes. To examine the mechanisms underlying hippocampal coding, we measured the intracellular dynamics of place cells by combining in vivo whole cell recordings with a virtual reality system. Head-restrained mice, running on a spherical treadmill, interacted with a computer-generated visual environment to perform spatial behaviors. Robust place cell activity was present during movement along a virtual linear track. From whole cell recordings, we identified three subthreshold signatures of place fields: (1) an asymmetric ramp-like depolarization of the baseline membrane potential; (2) an increase in the amplitude of intracellular theta oscillations; and, (3) a phase precession of the intracellular theta oscillation relative to the extracellularly-recorded theta rhythm. These intracellular dynamics underlie the primary features of place cell rate and temporal codes. The virtual reality system developed here will enable new experimental approaches to study the neural circuits underlying navigation.

Hippocampal place cells encode spatial information during navigation using rate and temporal codes[1,2]. The rate code refers to a selective increase in firing rate at a specific location in a local environment[3], and the temporal code includes the precise timing of spikes relative to the hippocampal theta rhythm (phase precession)[4–6]. To explain the origins of these codes, theoretical network and cellular models have been proposed[4,7–16]. These models make differing predictions about the subthreshold membrane potential dynamics of place cells (Fig. 1A–E, G–I), reflecting differences in the proposed mechanisms underlying hippocampal coding. The predicted intracellular dynamics include steady oscillations at theta frequencies that reflect a global hippocampal theta rhythm[7–9,12] (Fig. 1E), modulation of the amplitude and frequency of membrane potential theta oscillations[4,10,11,13–15] (Fig. 1B–D), and ramps of depolarization of the baseline membrane potential[7–10,12,13] (Fig. 1D–E). To account for phase precession, these models also make differing predictions about the relationship between intracellular theta oscillations

and the local field potential (LFP) theta rhythm. Models predict either that intracellular theta is phase-locked to the LFP theta rhythm with phase precession resulting from a ramp of depolarization[7–9,12] or that intracellular theta in the place field is at a higher frequency than the LFP rhythm[4,10,11,13–15] (Fig. 1G–I).

Because the models of hippocampal coding make differing predictions of subthreshold membrane potential dynamics, it is possible to distinguish between these models through intracellular measurements from place cells during spatial behaviors. However, intracellular recording methods require a level of mechanical stability that is difficult to obtain in freely moving animals[17,18]. Previously, head restraint on a spherical treadmill has been used to reduce brain motion necessary for optical imaging at cellular resolution in awake, mobile mice[19]. In addition, a previous study has provided evidence that body-tethered rats can navigate through virtual environments[20]. We reasoned that these could be combined to facilitate whole cell recordings to reveal the intracellular dynamics of place cells and thus distinguish between models of hippocampal coding.

Spatial behavior in a virtual environment

The visual virtual reality system for head-restrained mice we developed is shown in Fig. 2A. A mouse runs on top of an air-supported spherical treadmill with its head held fixed in space using a head plate. The mouse is surrounded by a toroidal screen that covers a wide area to accommodate a rodent's large field of view[20]. An image is projected onto the screen from a digital light processing projector via an angular amplification mirror[21] (Fig. 2A, Supplementary Fig. 1; Methods). To control the virtual reality system, we developed custom software using the open source Quake2 video game engine. The visual display was updated based on movements of the animal, measured as rotations of the spherical treadmill using an optical computer mouse (Methods).

Can head-restrained mice perform visually-guided spatial behaviors in a virtual environment? We trained water-scheduled mice using operant conditioning to run along a virtual linear track (180 cm long) that had proximal and distal walls with varying patterns for location cues (Fig. 2B). Mice were able to turn around at any position along the track's length. Small water rewards were given for running between reward zones located at opposite ends of the track; consecutive rewards were not available at a single reward site. After several training sessions, mice ran large total distances with high peak running speeds (Session 4: total distance = 217 ± 97 m per 40 minutes, peak speed = 41 ± 17 cm/s over a 2 s period, mean ± sd). Individual mice received rewards at increasing rates over time (Fig. 2C–D). Also, the average distance traveled between rewards decreased across sessions (Fig. 2E), consistent with learning of the task. After ten training sessions, mice ran 281 ± 53 cm between rewards, on average, approaching an ideal performance of 180 cm/reward (i.e. the distance between reward zones). These data suggest that head-restrained mice can perform visually-guided spatial behaviors in a virtual reality environment.

Place cells in a virtual environment

Although our behavior results suggest that mice have a spatial understanding of the virtual environment, the activation of navigation circuits during these behaviors would provide

additional evidence. To assess the function of the hippocampal place cell circuitry, we performed acute extracellular recordings in dorsal hippocampus from CA1 pyramidal neurons (Fig. 3A). We recorded during behavior along the virtual linear track from mice that had been trained for at least five days. Recorded cells had spiking patterns characteristic of hippocampal pyramidal neurons. Cells fired bursts of action potentials at high frequencies (>50 Hz) with decreasing spike amplitudes[22–24]; bursts occurred at intervals of ~130 ms corresponding to theta frequencies of ~6–10 Hz (Fig. 3A–B). In all mice tested, we identified units with place cell characteristics (23 cells from 8 mice, Methods). Place cells had low overall firing rates with spatially modulated firing patterns (overall firing rate = 1.0 ± 0.3 Hz; in-field firing rate = 4.7 ± 2.6 Hz; out-of-field firing rate = 0.6 ± 0.2 Hz; Fig. 3C). Place field size was, on average, 41 ± 14 cm. Place cell activity in some cases had directionality, with different place fields and firing rates depending on the direction of running[25] (directionality index = 0.6 ± 0.2, Methods; Fig. 3C). We also measured phase precession of spike times relative to LFP theta oscillations during runs through the place field[4,5]. Spike times shifted to earlier phases during movement through the place field, and the phase and position of spikes were negatively correlated (Phase = –72.6 ± 47.7 degrees between the first and last eighth of the field, P < 0.01; C = –0.17 ± 0.09 between phase and position, P < 0.01; n = 10 place fields, 8 cells, 3 mice; Fig. 3D–E). These firing rate and phase precession characteristics along the virtual linear track are highly similar to those measured in freely-moving mice in real environments[26–29]. These data therefore demonstrate that hippocampal place cell circuitry is operational in head-restrained mice during visually-guided spatial behaviors in the virtual reality system.

Intracellular dynamics of place cells

We next developed methods to measure the intracellular activity of hippocampal neurons during behavior along the virtual linear track. Because the mouse's head is stationary in the virtual reality setup, we were able to perform whole cell patch clamp recordings using a patch electrode with a long taper mounted on a standard micromanipulator positioned outside the mouse's field of view (see Methods). We obtained recordings in awake mice[17,18,30,31] as they ran on the spherical treadmill. Recordings lasted many minutes on average (7.7 ± 3.8 minutes; maximum, 20.4 minutes; n = 46 cells from 15 mice), during which time mice ran long distances at high speeds in the virtual environment (27 ± 5 m per minute; total distance, range: 125–458 m). We did not detect any major motion-induced artifacts in the electrophysiology recordings. Recordings could be performed from the same animal across multiple days (6 days per mouse;   3 days per hemisphere).

A subset of our whole cell recordings was made from place cells (overall firing rate = 2.2 ± 0.4 Hz; in-field firing rate = 7.3 ± 1.4 Hz; out-of-field firing rate = 1.5 ± 0.4 Hz; field size = 43 ± 13 cm; n = 8 cells from 8 mice; Fig. 4A–B, Supplementary Figs. 2A, 3). Approximately 36% of spontaneously active putative pyramidal neurons had a place field along the virtual track, which is consistent with estimates from extracellular recordings and immediate early gene studies in rats exploring real environments[32,33] (see Methods). Place cells recorded intracellularly fired in theta bursts (high frequency bursts at >50 Hz occurring at theta frequencies of ~6–10 Hz), resulting in ISI distributions with peaks at <10 ms and ~130 ms, consistent with our extracellular measurements (c.f. Supplementary Fig. 4 and Fig.

3B). The individual action potentials during a theta burst often occurred during the ascending phase of an underlying theta oscillation (Fig. 5A,D). Spike amplitudes decreased within a burst without a change in the peak potential of the spike, suggesting that depolarizing intracellular oscillations contribute to intra-burst decreases in spike amplitude[34]. Whole cell recordings from place cells therefore can be obtained in head-restrained mice behaving in virtual environments.

From our whole cell recordings of place cell activity, we examined two types of membrane potential dynamics proposed by the theoretical models of place cell function: ramps of depolarization and modulation of theta oscillations (Fig. 1B–E, H–I). We first analyzed changes in the average baseline membrane potential during behavioral epochs inside and outside the place field. As a mouse approached the recorded cell's place field, the average membrane potential, excluding action potentials, increased in a ramp-like manner and remained elevated until the place field was passed (Fig. 4A). The ramp of depolarization often began before action potential firing in the place field commenced and in some cases reached a steady depolarization as large as ~10 mV (peak depolarization = 5.7 ± 2.9 mV; Fig. 4A, Supplementary Figs. 5, 6). These depolarization events occurred preferentially in place fields; the average membrane potential excluding action potentials was higher in place fields than outside of place fields ($V_{\text{in-field}} - V_{\text{out-of-field}} = 2.5 \pm 0.5$ mV, $P < 0.0001$; Fig. 4C–D, Supplementary Fig. 2B). Consistently, the baseline membrane potential and firing rate were strongly correlated ($C = 0.55 \pm 0.10$, $P < 0.001$). On complete runs through the place field, ramps of depolarization were asymmetric with the peak depolarization shifted toward the end of the field (position of the peak depolarization = 72 ± 24% of the distance through the field, $P < 0.05$ vs. 50%; slope before peak = 3.0 mV per place field length, slope after peak = 5.4 mV per field length, $P < 0.001$; Fig. 4E). In contrast, firing rates were symmetric within the place field (position of the peak firing rate = 52 ± 17% of the distance through the field, $P > 0.6$ vs. 50%; slope before peak = 13.3 Hz per place field length, slope after peak = 13.6 Hz per field length, $P > 0.4$; Fig. 4E), perhaps because firing rates were highest on the ascending part of a ramp depolarization[13] (Supplementary Fig. 7A). An asymmetric ramp-like depolarization of the baseline membrane potential therefore is a subthreshold signature of place fields.

We next examined the modulation of the amplitude and phase of membrane potential oscillations occurring at theta frequencies during runs along the virtual track. We measured intracellular theta oscillations by band-pass filtering our membrane potential recordings from 6–10 Hz, after action potentials were removed (Fig. 5A; Methods). When the mouse entered the recorded cell's place field, the amplitude of intracellular theta oscillations increased (Fig. 5A). Theta-band power in the membrane potential trace was higher in place fields than outside of place fields ($\text{Power}_{\text{in-field}} = 1.7 \pm 0.4$ mV2, $\text{Power}_{\text{out-of-field}} = 0.8 \pm 0.2$ mV2, $P < 0.01$; Fig. 5B–C, Supplementary Figs. 2C, 8). Consistently, theta oscillation amplitude and firing rate were highly correlated ($C = 0.61 \pm 0.09$, $P < 0.001$). In contrast, the amplitude of membrane potential theta oscillations was similar at all spatial locations for putative CA1 pyramidal neurons that did not have a place field (Supplementary Fig. 9) and for the LFP theta rhythm (Supplementary Fig. 10).

To examine the modulation of the phase of intracellular theta, we compared intracellular theta fluctuations with LFP theta oscillations. We began by looking for phase precession of spike times relative to membrane potential theta oscillations. The intracellular phases of spike times did not change during runs through the place field, and the phase and position of spikes were not correlated (Phase = 0.6 ± 10.4 degrees between the first and last eighth of the field, $P > 0.9$; C = -0.01 ± 0.08 between phase and position, $P > 0.6$; Fig. 5D–G). Because spike times advanced relative to LFP theta oscillations but not intracellular theta (c.f. Figs. 3D–E, 5D–E), it is predicted that a phase shift between LFP and intracellular theta occurs during place field traversals. We therefore performed simultaneous whole cell and LFP recordings to directly compare the phases of intracellular and extracellularly-recorded theta. During runs through the place field, the phase difference between intracellular and LFP theta shifted such that the intracellular theta oscillation phase precessed relative to the LFP theta rhythm (C = -0.26 ± 0.12 between LFP phase and position for the times of intracellular theta peaks; n = 2 cells from 2 mice; Fig. 5F–G, Supplementary Fig. 11A). Consistently, the frequency of intracellular theta oscillations in the place field was higher than the frequency of LFP theta fluctuations (measured as a ratio of periods of intracellular theta to periods of LFP theta; $Ratio_{in-field}$ = 0.97 ± 0.21, $P < 0.01$ vs. 1; frequency = 0.23 Hz given a mean LFP frequency of 7.4 Hz; see Methods, Supplementary Fig. 11B). In contrast, the frequencies of intracellular theta and LFP theta during epochs outside the place field were similar ($Ratio_{out-of-field}$ = 1.01 ± 0.22, $P > 0.2$ vs. 1; Supplementary Fig. 11B). Intracellular theta oscillations in place cells therefore were not constant in amplitude or phase (relative to LFP theta) throughout runs on the linear track; rather, membrane potential theta oscillations were dynamically modulated across positions in virtual space.

Ramp-like depolarizations of the membrane potential and increases in intracellular theta oscillation amplitude were present simultaneously, which can be demonstrated directly by filtering the membrane potential trace from DC-10 Hz (Fig. 1F). Consistently, intracellular theta power and the baseline membrane potential were highly correlated (C = 0.52 ± 0.07, $P < 0.001$; Figs. 4C, 5B, Supplementary Fig. 2B–C). To determine if ramps of depolarization trigger increases in theta amplitude, we injected ramps of current at the soma while the animal was running along the virtual track and measured changes in theta power. Theta power increased weakly with higher levels of depolarization; however, the increase in power was smaller than during runs through the place field ($P < 0.01$ at similar V values; c.f. Figs. 4C, 5B and Supplementary Fig. 7B). Ramp-like depolarizations of the membrane potential therefore were not sufficient to cause the increases in theta oscillation amplitude observed in place fields.

Our whole cell recordings revealed two additional subthreshold phenomena. First, in a fraction of our recordings we observed spikelets, brief small amplitude deflections of the membrane potential (2/8 place cells; amplitude = 7.4 ± 1.3 mV, full-width at half maximum = 1.6 ± 0.4 ms; 0.06 ± 0.05 spikelets per second; Supplementary Fig. 12A)[35]. Second, bursts of action potentials were occasionally followed by large (~10–25 mV) depolarizations lasting up to 50–100 ms[23] (Supplementary Fig. 12B). These events sometimes contained broadened spikes of reduced amplitude, consistent with Ca^{2+} spikes recorded in slices[36]. Further analysis is required to assess the prevalence, significance, and mechanisms of these events.

Discussion

Here we have developed a visual virtual reality system in which head-restrained mice performed spatial behaviors along a virtual linear track. Hippocampal place cell activities were triggered during runs along the track with properties similar to those recorded in real environments. Because the mouse was head-restrained, we were able to obtain whole cell recordings lasting many minutes in awake mice using standard patch clamp techniques. Furthermore, this set-up can likely be combined with two-photon laser scanning microscopy, which has previously been performed in mice running on the spherical treadmill[19]. Virtual reality also offers the ability to design highly custom environments and to rapidly manipulate these environments through software. We therefore anticipate that our virtual reality system will make possible new types of experiments exploring spatial information encoding.

We identified three subthreshold signatures of place fields: an asymmetric ramp-like depolarization of the baseline membrane potential, an increase in the amplitude of membrane potential theta oscillations, and a phase precession of intracellular theta relative to LFP theta, such that spike times advanced relative to LFP theta but not intracellular theta (Figs. 1F, 4, 5). These findings appear inconsistent with the mechanisms underlying dual oscillator models[2,4,14], network models[7–9], and an experience-dependent model[12] of hippocampal rate and temporal coding because each model predicts membrane potential dynamics that differ significantly from our observed subthreshold signatures (Figs. 1B–C, E–H). Our data are most consistent with a soma-dendritic interference (SDI) model that proposes interactions between a spatially-independent inhibitory oscillatory input near the soma and a spatially-dependent (increasing in the place field) and temporally patterned (at theta) dendritic excitatory input[10,11,13,15]. With an appropriate choice of conductances[15], the SDI model predicts, in the place field, ramp-like depolarizations (Figs. 1D, 4), an increase in theta amplitude (Figs. 1D, 5A–C), and precession of intracellular theta relative to extracellular theta (Figs. 1I, 5F–G). We note, however, that we observed an asymmetric ramp-like depolarization (Fig. 4E), which may be important for phase precession across the entire place field[12], compared with a symmetric ramp proposed in this model. We do not exclude the possibility that revised forms of other models could potentially explain the intracellular dynamics we observed. Additional experiments will be necessary to define and quantify the cellular and synaptic mechanisms underlying the intracellular dynamics we measured, including in the context of the entorhinal cortex[2,16,37], and to establish their causal relationship to rate and temporal codes in the hippocampus. The virtual reality system developed here, combined with electro- and opto-physiological methods, will likely facilitate this analysis.

Methods Summary

A virtual reality system was designed using an air-supported spherical treadmill for head-restrained mice[19] in combination with a projection-based visual display system[20], in which a toroidal screen presented an image from a projector via an angular amplification mirror[21]. Custom software to control the virtual reality system was developed based on the Quake2 game engine. Rotations of the spherical treadmill, measured by an optical computer mouse,

were used to update the visual display. Water-scheduled C57BL/6J mice (8–12 weeks old) were trained using operant conditioning to run from end-to-end of a virtual linear track (180 cm long) to obtain water rewards. For electrophysiology measurements, a small craniotomy (~0.5 mm diameter) was made centered over dorsal hippocampus (2.2 mm caudal, 1.7 lateral to bregma). The craniotomy was sealed with silicone grease and then covered with silicone elastomer to allow recordings across multiple days. Extracellular recordings were made using a glass electrode (filled with 0.5 M NaCl, ~2.5 MΩ pipette resistance) mounted on a micromanipulator positioned behind the mouse. Whole cell recordings were obtained using standard blind patch methods. Patch pipettes were pulled with a long taper (~100 μm diameter at 1 mm from the tip), to minimize damage to the overlying cortical tissue, and were mounted on a micromanipulator positioned outside the field of view. Firing rate maps were calculated for 80 spatial bins along the virtual track as the number of spikes in a bin divided by the time spent in that bin. Changes in baseline membrane potential in the place field were measured from membrane potential traces excluding spikes. Theta oscillations were analyzed following band-pass filtering (6–10 Hz) of the membrane potential recording using a linear phase finite impulse response filter.

Methods

Virtual reality set-up

The virtual reality system (Fig. 2A, Supplementary Fig. 1) was designed around an air-supported spherical treadmill (8 inch diameter Styrofoam ball) for head-restrained mice that was previously used for in vivo optical imaging at cellular resolution[19]. A projection-based visual display, similar to the system used in a body-tethered rat virtual reality system[20], presented a computer rendered scene with a 270 degree horizontal field of view and a vertical field from +60 to −20 degrees relative to the mouse's head. The toroidal screen displayed the 2D image from a Mitsubishi HC3000 digital light processing (DLP) projector reflected off of a 15 cm diameter round mirror and a 15 cm diameter angular amplification mirror (AAM)[21] with an angular amplification factor of 12. The AAM was machined out of aluminum using a CNC machine and then polished by hand. The screen was ~46 cm tall and ~80 cm in outer diameter and was constructed out of a semi-reflective nylon material (Rose Brand fabrics) supported by a frame of stainless steel rods. Water rewards were delivered via a solenoid valve (NResearch) attached to a water feeding tube (Popper and Sons) positioned directly in front of the animal's mouth such that the mouse could lick the meniscus. Rotations of the Styrofoam ball were measured by an optical computer mouse (Logitech MX1000) that was positioned below the field of view in front of the animal at the point where the ball's equator intersected the animal's rostral-caudal body axis. A computer running Labview used USB-communicated signals from the optical mouse to compute low-pass filtered ball rotational velocity around both the horizontal axis (perpendicular to the body axis) and vertical axis. These velocities were then output as analog control voltages using a D/A converter (National Instruments) and used as input control signals to a separate computer running the virtual reality software.

The virtual reality software we developed was based on the open source Quake2 game engine (id software), using code ported to Visual Studio 2008. The rendering engine was

modified, using cube map texturing in OpenGL graphics38, to display a "fisheye" transform of the perspective of the virtual player, such that the image reflected off the AAM and displayed on the screen had the geometrically correct perspective for the mouse on the ball. Software to control the water reward system, input information on ball rotation velocity, and output voltages proportional to position and view angle within the environment was also developed by adding A/D and D/A control to the game engine, using National Instruments multifunction cards. Ball velocity around the vertical axis was used as a control signal for changing view angle in the virtual environment, while velocity around the horizontal axis was used as a control signal for forward and backward movement. Other open source gaming software (Quark, http://quark.planetquake.gamespy.com/) was used to build the virtual linear track. To synchronize behavior data with electrophysiology recordings, an independent computer with a Digidata 1440A interface running Clampex software (Molecular Devices) digitized and stored real time information about the mouse's location in the virtual environment together with solenoid (water reward) control signals, ball rotational velocities, and electrophysiological data.

Behavioral training

Eight to twelve week old male C57BL/6J mice (Jackson Labs) were used for all experiments. C57BL/6J mice were selected because they have good vision compared to other inbred strains39 and are a common background strain for transgenic mice. All experimental procedures were performed in compliance with the Guide for the Care and Use of Laboratory Animals (http://www.nap.edu/readingroom/books/labrats/) and were approved by Princeton University's Institutional Animal Care and Use Committee. Prior to behavioral training, titanium head plates with a large central opening (2.5 cm wide × 0.9 cm long × 0.08 cm thick; central opening: 0.89 cm wide × 0.61 cm long) were implanted on mice and affixed to the skull using dental cement (Metabond, Parkell). Sites for future craniotomies over the left and right dorsal hippocampi were marked using stereotactic coordinates (2.2 mm caudal, 1.7 mm lateral to bregma). Following head plate implantation, mice were placed on a water schedule in which they received 1 mL of water per day. Body weights were checked to ensure mice were ~80% of their pre-water-restriction weight40,41.

After at least five days of water scheduling, behavior training began. In each training session, mice were placed on the experimental apparatus with their head fixed in place. The head was centered over the middle of the Styrofoam ball with the headplate ~2.6 cm from the top of the ball. A lick tube to deliver water rewards was positioned in front of the mouse's mouth. The water rewards earned during behavior were included in the mouse's daily water allotment such that a mouse received exactly 1 mL of water per day. Each training session (one per day) lasted 45 minutes with the virtual reality system turned on for all sessions. The first several sessions mostly involved acclimation to the apparatus and learning to run on the spherical treadmill.

Mice were trained to perform behaviors along a virtual linear track. The virtual track was 180 cm long and 9 cm wide, measured as the number of rotations of the Styrofoam ball to move from one end of the track to the other times the circumference of the ball. The effective width of the track (i.e. the distance the mouse could actually move) was ~1 cm,

rather than 9 cm, because in Quake2 the player is surrounded by a bounding box that gives him a fixed width. The track had short proximal walls with different textures for each third of the track (0–60 cm: white with black dots, 61–120 cm: vertical white and black stripes, 121–180 cm: black with white dots). The proximal walls at the ends of the track were green with black dots to mark the reward zones. Tall distal walls were positioned at 60 cm (horizontal black and white stripes) and 120 cm (green with black crosses). The floor and ceiling were black throughout the track. Green was selected as the only non-black or white color because electrophysiological and behavioral data indicate that mice can detect wavelengths of ~500 nm42. Mice received small water rewards (4 μL) for running between reward zones positioned at opposite ends of the track (zone 1 postion: 0–9 cm; zone 2 position: 171–180 cm). After receiving a reward at one reward zone, the mouse then had to run to the other reward zone to receive the next reward; two consecutive rewards could not be obtained from a single reward site. Linear track behavioral data (Fig. 2C–E) were from mice trained only on the linear track. Some animals used for electrophysiology recordings were trained in other virtual environments prior to training in the linear track. During electrophysiology experiments, behavioral performance was in some cases degraded due to satiation from water rewards and because the visual display was turned off while patch pipettes were changed.

Electrophysiology

After at least five training sessions on the virtual linear track, a small craniotomy (~0.5 mm diameter) was made over the left hippocampus (2.2 mm caudal, −1.7 mm lateral to bregma). The dura was left intact for both extracellular and intracellular recordings. Because behavioral performance was degraded on the day of surgery and anesthesia, electrophysiology recordings were performed starting the following day. To preserve the craniotomy across days, it was covered with silicone grease (Dow Corning) and then with a layer of silicone elastomer (Kwik-Sil, World Precision Instruments) until the time of recording. Extracellular recordings (Fig. 3, Supplementary Fig. 10) were made using a single glass electrode filled with 0.5 M NaCl (~2.5 MΩ pipette resistance). The electrode was mounted vertically (perpendicular to the surface of the brain) on a micromanipulator (Sutter MP285) that was positioned behind the mouse and thus outside the mouse's field of view. The reference electrode was positioned outside the craniotomy in extracellular saline containing (in mM): 150 NaCl, 2.5 KCl, 10 HEPES (pH 7.4). Signals were electronically filtered between 500 Hz and 7.5 kHz and digitized at 20 kHz. For measurements of the LFP and phase precession, signals were electronically filtered between 2 Hz and 10 kHz; spikes and the LFP were recorded on the same electrode. The position of the top of the brain was noted as a large resistance increase when the electrode made contact with the dura. As the electrode was advanced through cortex, spikes were present in each layer. Upon entering the external capsule, a change in the recording was noted, especially from changes in sound quality using an audio monitor. The CA1 cell body layer was ~200 μm beneath the external capsule and was characterized by strongly theta-modulated spiking. Putative pyramidal neurons were found as units firing complex bursts separated at theta frequencies22. In all animals CA1 recordings were made at a depth of ~1.1 mm; cells were found reproducibly at this depth across multiple electrodes and days. To confirm that this recording position was in the CA1 cell body layer, in a separate experiment we electroporated Alexa 488 dextran (5%

wt/vol in extracellular saline, 4 μA pulses, 25 ms pulse duration, 600 pulses at 2 Hz) using a recording pipette and found bright labeling of CA1 cell bodies in histology sections. At this depth, we searched for well-isolated units of large amplitude and recorded their activity for ~15–30 minutes, which was enough time for the mouse to sample thoroughly the virtual linear track. Spikes were sorted offline using a threshold analysis. At most one unit was isolated from a single recording. To check the quality of unit isolation, we overlaid all spike waveforms to make sure that they matched by visual inspection (Fig. 3A), and we plotted ISI distributions to make sure no spikes fell within the refractory period (<1–2 ms; Fig. 3B). Extracellular recordings were made from a total of 8 mice. In some cases a second craniotomy was made over the right hemisphere to extend the number of recording sessions from a single animal. Recordings were made for up to 4 days from the same craniotomy. Place cells were found in every mouse tested.

Whole cell recordings were made using the same experimental setup as for extracellular recordings. Pipettes (~5–7 MΩ) were filled with internal solution containing (in mM): 135 K-gluconate, 10 HEPES, 10 Na_2-phosphocreatine, 4 KCl, 4 MgATP, 0.3 Na_3GTP (pH 7.25 with KOH, 285 mOsm). We pulled pipettes with a long taper (~100 μm diameter at 1 mm from the tip) to minimize damage to the overlying cortical tissue and to reduce compression of the tissue while advancing the pipette. The pipette was mounted vertically on a standard micromanipulator (Sutter MP285) positioned outside the mouse's field of view; special methods to anchor the pipette[17,18] were not necessary. We used standard blind patch methods to obtain whole cell recordings[30]. In brief, we applied ~250 mbar of positive pressure while moving the pipette through the cortex and reduced the pressure to ~15 mbar while searching for cells in the hippocampus. The CA1 cell body layer was located using a depth coordinate obtained from extracellular recordings in the same animal. We attempted to form a seal when we observed large (~50%), reproducible increases in pipette resistance. Recordings were made in current clamp mode with no holding current. Membrane potential values were corrected for liquid junction potentials. We obtained recordings lasting longer than 3 minutes from 46 cells from 15 mice, with a peak success rate of approximately one such recording in every five attempts. Recordings were abandoned when we observed large increases in resting potential or large decreases in spike amplitude. We obtained whole cell recordings for up to 3 days from the same craniotomy. Whole cell recordings from place cells lasted on average 7.1 ± 2.8 minutes and had series resistances of 48 ± 16 MΩ, input resistances of 98 ± 23 MΩ, and resting membrane potentials of −67 ± 4 mV. Firing rates from place cells recorded intracellularly tended to be higher than those recorded extracellularly, both inside and outside the place field, potentially because a fraction of spikes measured extracellularly were lost during spike sorting. All other place cell parameters (e.g. field size, ISI distribution) were similar between cells recorded extracellularly and intracellularly. Although we cannot exclude possible effects of dialysis of the cell during whole cell measurements, such effects are likely small due to short recording durations and relatively high series resistances. In experiments to assess the connection between ramps of depolarization and changes in theta oscillation amplitude (Supplementary Fig. 7), ramps of current (4 seconds duration, 1–1.5 nA at the peak) were injected at the soma following 11 seconds without current injection. Only trials in which the animal was running at greater than 10 cm/s were analyzed.

To perform whole cell and extracellular recordings simultaneously (Fig. 5F–G, Supplementary Fig. 11), we mounted two glass electrodes on separate micromanipulators, which were both positioned behind the mouse, and advanced the electrodes independently through separate craniotomies on the same hemisphere. Whole cell recordings were made at the standard coordinates as described above. The extracellular recording electrode (filled with 0.5 M NaCl) was mounted at a 40 degree angle relative to the midline and a 45 degree angle with respect to the vertical. The craniotomy for the extracellular electrode was positioned caudal and either lateral for the left hemisphere or medial for the right hemisphere relative to the craniotomy for intracellular recordings. The tip of the extracellular electrode was positioned at a depth of ~1.2 mm and ~250 μm caudal to the center of the craniotomy for whole cell recordings. The extracellular recordings were filtered between 1 Hz and 10 kHz.

From our 46 hippocampal whole cell recordings, 41 cells were spontaneously active (overall firing rate > 0.05 Hz). We classified 7 of the spontaneously active cells as interneurons based on high overall firing rates (>5 Hz) and the absence of complex spike bursts. The remaining 34 spontaneously active cells were categorized as pyramidal neurons. To estimate the fraction of spontaneously active pyramidal neurons that had a place field along the virtual linear track, we considered only those recordings during which the animal visited each of the 80 spatial segments at least 3 times, with visits separated by at least 2 seconds in time. We estimate that 36% of spontaneously active pyramidal neurons had place fields in the virtual environment (8 out of 22 cells). During whole cell place cell recordings, the place field was visited 20 ± 8 times on average, with visits separated by at least 2 seconds in time.

Data analysis

To create firing rate maps (Figs. 3C, 4B, Supplementary Fig. 2A), we divided the virtual linear track into 80 bins (2.25 cm each) and calculated the firing rate as the total number of spikes in a bin divided by the total amount of time spent in a bin. The maps were smoothed using a five point Gaussian window with a standard deviation of one. Periods in which the mouse ran slower than 5 cm/s, averaged over a 2 second window, were removed from the analysis. To identify place fields, we found groups of adjacent bins with firing rates greater than 0.25 times the rate in the peak bin. We selected only those fields that were larger than 8 bins (18 cm) in length, had mean in-field firing rates of greater than 1.5 Hz, and had mean in-field firing rates more than 3 times larger than the mean out-of-field firing rate. To verify that place fields were a statistically significant increase in firing rate, we performed a bootstrap shuffle test. We shuffled the times of spikes in 10 second segments, calculated new firing rate maps using the unshuffled bin dwell times, and then checked for a place field using the above-stated criteria. This procedure was repeated 1000 times per place cell recording. We called a cell a place cell only if a place field was found in the unshuffled data and in fewer than 2% of the shuffled tests ($P < 0.02$). Across the place cells we recorded, we found place fields at all positions along the linear track. Spikes were separated into leftward and rightward runs based on the head direction of the animal with regard to the virtual track (measured as the player's view angle in Quake2). A directionality index for firing based on firing rates in leftward and rightward directions (FR_{left}, FR_{right}) was defined as |

FR$_{left}$−FR$_{right}$|/(FR$_{left}$+FR$_{right}$). A directionality index of 0 indicates identical firing in both directions, whereas an index of 1 indicates firing in one direction only.

To quantify the average baseline membrane potential as a function of position along the virtual track (Fig. 4C, Supplementary Fig. 2B), we first removed the contribution of action potentials by discarding all time points between 4 ms before and 7 ms after an action potential's peak. We then created a map of membrane potential values by grouping the membrane potentials into 80 spatial bins along the track and calculating an average membrane potential for each bin. The membrane potential map was smoothed using a five point Gaussian window with a standard deviation of one. Large, long-lasting depolarizations of the baseline membrane potential occurred infrequently outside the place field (2.3 ± 1.3 events per recording for depolarizations of greater than 2 mV lasting longer than 0.5 seconds).

To analyze ramps of depolarization during complete runs through the place field (i.e. the mouse did not turn around inside the place field), we calculated changes in membrane potential (V) after action potentials were removed (Fig. 4E, Supplementary Figs. 5, 6B). We defined the baseline membrane potential as the mean membrane potential from 500 ms to 1 s before the mouse entered the place field and subtracted this baseline from all membrane potential values during the run to get V values. The peak V during a run through the place field (Supplementary Fig. 6B) was calculated after smoothing the V values over a sliding window of length 50 ms such that the peak value was representative of the ramp-like depolarization rather than brief, high frequency depolarizations. To analyze the symmetry of firing rates and ramps of depolarization in place fields (Fig. 4E), we considered runs starting half the place field's width before the place field and ending half the place field's width beyond the place field (total length was twice the length of the place field). Because place fields varied in size between cells and runs through the field differed in duration, we divided each run into 60 equally sized spatial bins and calculated the mean firing rates and V for each 1/60th of the run (i.e. 15 spatial bins before the place field, 30 bins in the field, and 15 bins after the field). All runs through the field were plotted with increasing track position values so that runs in opposite directions could be combined.

To analyze subthreshold theta oscillations (Fig. 5, Supplementary Figs. 2C, 7, 9), spikes were removed over a window of 3 ms preceding and 5 ms following the peak and were replaced using linear interpolation. The resulting trace was then band-pass filtered between 6–10 Hz (a peak in the ISI distribution) using a linear phase finite impulse response (FIR) filter with a Hamming window of width 1 second (Matlab function fir1). To create a map of theta power along the virtual track, power was calculated as the mean of the squared amplitude for a sliding window of length 1 second for the entire recording, with the center of the window providing the position along the track. The power values were grouped into 80 spatial bins along the track and smoothed using a five point Gaussian window with a standard deviation of one. Power spectra for epochs in and out of the place field were obtained using multi-taper spectral analysis methods (Chronux toolbox, http://chronux.org; Supplementary Fig. 8). Running speed, which can influence theta oscillations43, was similar inside and outside the place field (in-field speed = 49 ± 6 cm/s, out-of-field speed = 47 ± 4

cm/s, P > 0.7). LFP theta oscillations were present when the animal was running (Fig. 3D, Supplementary Fig. 10) and absent when the animal was resting.

To analyze phase precession (Figs. 3D–E, 5D–G), we considered complete runs through the place field (i.e. the animal did not turn around in the field) that had at least 5 spikes and in which the animal ran faster than 10 cm/s. Only cells with more than 40 total spikes in the place field were included. Extracellular or intracellular (after removing spikes) voltage traces were band-pass filtered between 6–10 Hz using an FIR filter. To assign a phase to a spike occurring at time t, we identified, in the filtered trace, the times of the peaks immediately preceding and following the spike (t_1 and t_2, respectively) and calculated the phase as $360 \times (t - t_1)/(t_2 - t_1)$. We circularly shifted the phase of the spikes in 1° steps from 0° to 360°, continuing across the 360° border, and fit a linear regression line to the phase vs. position plot at each rotation[4,37]. We found the rotation with the best fit, such that the sum of squared errors between the fit line and data was minimized, and used the correlation coefficient between phase and position at this rotation as a measure of phase precession. All phase values are from the raw data in relation to theta phase, with 0 degrees indicating the peak. To measure the precession of intracellular theta relative to extracellular theta (Fig. 5G), we first identified the times of the peaks of the filtered (6–10 Hz) membrane potential trace during runs through the place field. For each peak of intracellular theta, we found the corresponding phase of the simultaneously recorded extracellular theta and the position of the mouse along the virtual track and followed the same procedures that were used for the analysis of the phase precession of spike times. To quantify the change in times between intracellular theta peaks and LFP theta peaks during place field traversals (Supplementary Fig. 11A), we found the time difference between the first LFP theta peak and the first intracellular theta peak in the place field, the time difference between the second LFP theta peak and the second intracellular theta peak, and so on. To quantify frequency differences between intracellular and LFP theta (Supplementary Fig. 11B), we calculated the ratio of the period of the first intracellular oscillation to the period of the first LFP oscillation, the ratio of the period of the second intracellular oscillation to the period the second LFP oscillation, and so on using peaks from the filtered (6–10 Hz) traces. We determined these ratios for complete runs through the place field and 3 second long epochs outside the place field.

Data are presented as mean ± standard deviation unless noted otherwise. P values are from two-tailed t-tests unless stated otherwise. Correlation coefficients (C) are from Pearson's correlations.

Supplementary Material

Refer to Web version on PubMed Central for supplementary material.

Acknowledgments

References

1. Moser EI, Kropff E, Moser MB. Place Cells, Grid Cells, and the Brain's Spatial Representation System. Annu Rev Neurosci. 2008; 31:69–89. [PubMed: 18284371]

2. O'Keefe J, Burgess N. Dual phase and rate coding in hippocampal place cells: theoretical significance and relationship to entorhinal grid cells. Hippocampus. 2005; 15:853–866. [PubMed: 16145693]

3. O'Keefe J, Dostrovsky J. The hippocampus as a spatial map. Preliminary evidence from unit activity in the freely-moving rat. Brain Res. 1971; 34:171–175. [PubMed: 5124915]

4. O'Keefe J, Recce ML. Phase relationship between hippocampal place units and the EEG theta rhythm. Hippocampus. 1993; 3:317–330. [PubMed: 8353611]

5. Skaggs WE, McNaughton BL, Wilson MA, Barnes CA. Theta phase precession in hippocampal neuronal populations and the compression of temporal sequences. Hippocampus. 1996; 6:149–172. [PubMed: 8797016]

6. Buzsaki G. Theta oscillations in the hippocampus. Neuron. 2002; 33:325–340. [PubMed: 11832222]

7. Tsodyks MV, Skaggs WE, Sejnowski TJ, McNaughton BL. Population dynamics and theta rhythm phase precession of hippocampal place cell firing: a spiking neuron model. Hippocampus. 1996; 6:271–280. [PubMed: 8841826]

8. Jensen O, Lisman JE. Hippocampal CA3 region predicts memory sequences: accounting for the phase precession of place cells. Learn Mem. 1996; 3:279–287. [PubMed: 10456097]

9. Wallenstein GV, Hasselmo ME. GABAergic modulation of hippocampal population activity: sequence learning, place field development, and the phase precession effect. J Neurophysiol. 1997; 78:393–408. [PubMed: 9242288]

10. Kamondi A, Acsady L, Wang XJ, Buzsaki G. Theta oscillations in somata and dendrites of hippocampal pyramidal cells in vivo: activity-dependent phase-precession of action potentials. Hippocampus. 1998; 8:244–261. [PubMed: 9662139]

11. Magee JC. Dendritic mechanisms of phase precession in hippocampal CA1 pyramidal neurons. J Neurophysiol. 2001; 86:528–532. [PubMed: 11431530]

12. Mehta MR, Lee AK, Wilson MA. Role of experience and oscillations in transforming a rate code into a temporal code. Nature. 2002; 417:741–746. [PubMed: 12066185]

13. Harris KD, et al. Spike train dynamics predicts theta-related phase precession in hippocampal pyramidal cells. Nature. 2002; 417:738–741. [PubMed: 12066184]

14. Lengyel M, Szatmary Z, Erdi P. Dynamically detuned oscillations account for the coupled rate and temporal code of place cell firing. Hippocampus. 2003; 13:700–714. [PubMed: 12962315]

15. Gasparini S, Magee JC. State-dependent dendritic computation in hippocampal CA1 pyramidal neurons. J Neurosci. 2006; 26:2088–2100. [PubMed: 16481442]

16. Maurer AP, McNaughton BL. Network and intrinsic cellular mechanisms underlying theta phase precession of hippocampal neurons. Trends Neurosci. 2007; 30:325–333. [PubMed: 17532482]

17. Lee AK, Manns ID, Sakmann B, Brecht M. Whole-cell recordings in freely moving rats. Neuron. 2006; 51:399–407. [PubMed: 16908406]

18. Lee AK, Epsztein J, Brecht M. Head-anchored whole-cell recordings in freely moving rats. Nat Protoc. 2009; 4:385–392. [PubMed: 19247288]

19. Dombeck DA, Khabbaz AN, Collman F, Adelman TL, Tank DW. Imaging large-scale neural activity with cellular resolution in awake, mobile mice. Neuron. 2007; 56:43–57. [PubMed: 17920014]

20. Holscher C, Schnee A, Dahmen H, Setia L, Mallot HA. Rats are able to navigate in virtual environments. J Exp Biol. 2005; 208:561–569. [PubMed: 15671344]

21. Chahl JS, Srinivasan MV. Reflective surfaces for panoramic imaging. Appl Opt. 1997; 36:8275–8285. [PubMed: 18264368]

22. Ranck JB Jr. Studies on single neurons in dorsal hippocampal formation and septum in unrestrained rats. I. Behavioral correlates and firing repertoires. Exp Neurol. 1973; 41:461–531. [PubMed: 4355646]

23. Kandel ER, Spencer WA. Electrophysiology of hippocampal neurons. II. After-potentials and repetitive firing. J Neurophysiol. 1961; 24:243–259. [PubMed: 13751138]

24. Quirk MC, Wilson MA. Interaction between spike waveform classification and temporal sequence detection. J Neurosci Methods. 1999; 94:41–52. [PubMed: 10638814]

25. McNaughton BL, Barnes CA, O'Keefe J. The contributions of position, direction, and velocity to single unit activity in the hippocampus of freely-moving rats. Exp Brain Res. 1983; 52:41–49. [PubMed: 6628596]

26. Nakazawa K, et al. Hippocampal CA3 NMDA receptors are crucial for memory acquisition of one-time experience. Neuron. 2003; 38:305–315. [PubMed: 12718863]

27. Kentros CG, Agnihotri NT, Streater S, Hawkins RD, Kandel ER. Increased attention to spatial context increases both place field stability and spatial memory. Neuron. 2004; 42:283–295. [PubMed: 15091343]

28. Cacucci F, Wills TJ, Lever C, Giese KP, O'Keefe J. Experience-dependent increase in CA1 place cell spatial information, but not spatial reproducibility, is dependent on the autophosphorylation of the alpha-isoform of the calcium/calmodulin-dependent protein kinase II. J Neurosci. 2007; 27:7854–7859. [PubMed: 17634379]

29. Sun, LD.; Wilson, MA. PhD thesis. Massachusetts Institute of Technology; 2003. Impaired and enhanced spatial representations of the PSD-95 knockout mouse.

30. Margrie TW, Brecht M, Sakmann B. In vivo, low-resistance, whole-cell recordings from neurons in the anaesthetized and awake mammalian brain. Pflugers Arch. 2002; 444:491–498. [PubMed: 12136268]

31. Crochet S, Petersen CC. Correlating whisker behavior with membrane potential in barrel cortex of awake mice. Nat Neurosci. 2006; 9:608–610. [PubMed: 16617340]

32. Wilson MA, McNaughton BL. Dynamics of the hippocampal ensemble code for space. Science. 1993; 261:1055–1058. [PubMed: 8351520]

33. Guzowski JF, McNaughton BL, Barnes CA, Worley PF. Environment-specific expression of the immediate-early gene Arc in hippocampal neuronal ensembles. Nat Neurosci. 1999; 2:1120–1124. [PubMed: 10570490]

34. Henze DA, et al. Intracellular features predicted by extracellular recordings in the hippocampus in vivo. J Neurophysiol. 2000; 84:390–400. [PubMed: 10899213]

35. Kandel ER, Spencer WA. Electrophysiology of hippocampal neurons. IV. Fast prepotentials. J Neurophysiol. 1961; 24:272–285. [PubMed: 25286477]

36. Wong RK, Prince DA. Participation of calcium spikes during intrinsic burst firing in hippocampal neurons. Brain Res. 1978; 159:385–390. [PubMed: 728808]

37. Hafting T, Fyhn M, Bonnevie T, Moser MB, Moser EI. Hippocampus-independent phase precession in entorhinal grid cells. Nature. 2008; 453:1248–1252. [PubMed: 18480753]

38. Greene N. Environment mapping and other applications of world projections. IEEE Computer Graphics and Applications. 1986; 6:21–29.

39. Wong AA, Brown RE. Visual detection, pattern discrimination and visual acuity in 14 strains of mice. Genes Brain Behav. 2006; 5:389–403. [PubMed: 16879633]

40. Rinberg D, Koulakov A, Gelperin A. Sparse odor coding in awake behaving mice. J Neurosci. 2006; 26:8857–8865. [PubMed: 16928875]

41. Huber D, et al. Sparse optical microstimulation in barrel cortex drives learned behaviour in freely moving mice. Nature. 2008; 451:61–64. [PubMed: 18094685]

42. Jacobs GH, Neitz J, Deegan JF 2nd. Retinal receptors in rodents maximally sensitive to ultraviolet light. Nature. 1991; 353:655–656. [PubMed: 1922382]

43. Buzsaki G, Leung LW, Vanderwolf CH. Cellular bases of hippocampal EEG in the behaving rat. Brain Res. 1983; 287:139–171. [PubMed: 6357356]
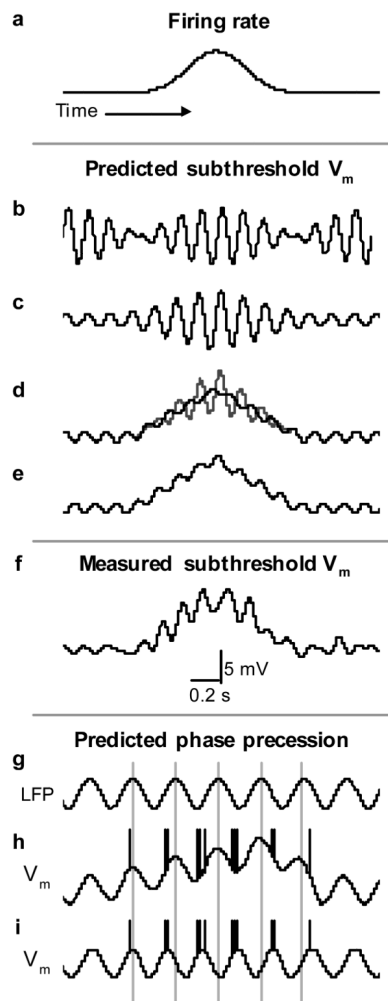
Figure 1. Predicted and measured subthreshold membrane potential dynamics during a run through a cell's place field

(A)Schematic of a place cell's firing rate during a run through its place field. All predicted and measured subthreshold membrane potential traces are aligned to the firing rate plot.

(B)Schematic of predicted subthreshold membrane potential dynamics from a dual oscillator interference model2,4. In this model, place cells receive two steady sets of rhythmic inputs occurring at different frequencies in the theta band. The interference between these oscillations results in a beat-like pattern of membrane potential fluctuations with the positive phase of the beat wave defining the place field. Note that the schematics in (B–E) only illustrate depolarizations and changes in theta amplitude.

(C)Schematic of predicted subthreshold membrane potential dynamics from a modified dual oscillator model14. Outside the place field, the two oscillations are 180° out of phase. Upon entering the place field, the frequency of one oscillation increases, resulting in a modulation of the summed oscillation.

(D)Schematic of predicted subthreshold membrane potential dynamics from a soma-dendritic interference model10,11,13,15. In this model, the cell receives somatic inhibitory inputs and dendritic excitatory inputs, both at theta frequencies. In the place field, the

excitatory drive increases, which is apparent as a ramp-like depolarization and an increase in the amplitude of excitatory theta oscillations. Depending on the conductances used in the model, the summed oscillation can have either increased (gray)15 or decreased (black)11 amplitude.

(E) Schematic of predicted ramps of depolarization of the baseline membrane potential. In a network model, the cell receives a place-related, symmetric ramp-like excitatory drive and inputs from neuronal assemblies with nearby place fields7–9. Another model proposes an asymmetric ramp of depolarization to combine rate and temporal codes12. Both models incorporate a steady membrane potential theta oscillation.

(F) Example of a subthreshold membrane potential recorded intracellularly from a place cell in a virtual environment. The membrane potential trace was filtered from DC-10 Hz, after spikes were removed, to illustrate the simultaneous occurrence of a ramp of depolarization and an increase in theta oscillation amplitude. The scale bars refer to the experimentally measured trace only.

(G)Schematic of the LFP theta rhythm. Peaks are marked by gray dashed lines.

(H)Schematic of a predicted relationship between intracellular theta and LFP theta to account for phase precession of spikes relative to LFP theta oscillations. Intracellular and LFP theta are the same frequency. Phase precession of spikes (black lines) occurs relative to both intracellular and LFP theta due to a ramp of depolarization7–9,12. An asymmetric ramp is shown. Note that the schematics in (H-I) are meant to illustrate only the relationships between spike times, intracellular theta, and LFP theta.

(I) Schematic of a predicted membrane potential trace in which intracellular theta is a higher frequency than LFP theta in the place field, resulting in phase precession of spikes relative to LFP theta but not intracellular theta2,4,10,11,13–15.
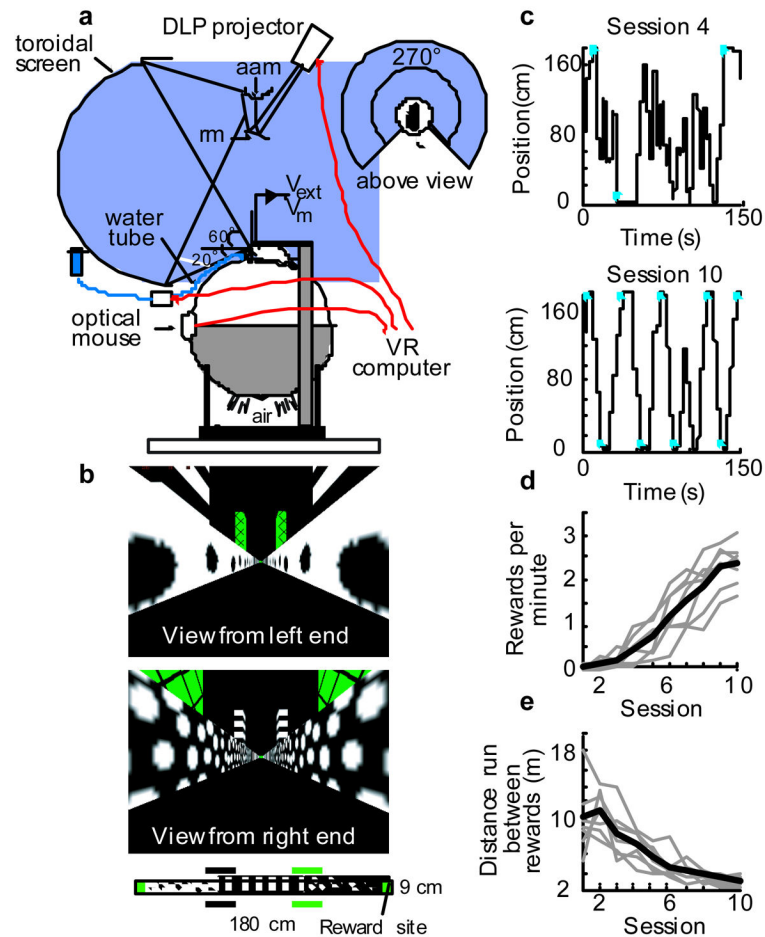
Figure 2. Spatial behaviors in a virtual reality environment

(A) Schematic of the experimental set-up. A head-restrained mouse runs on an air-supported spherical treadmill. An image from a DLP projector is displayed on a toroidal screen (−20 to +60 degrees vertically, 270 degrees horizontally) via a reflecting mirror (rm) and an angular amplification mirror (aam). Movements of the treadmill are measured using an optical computer mouse. Water rewards are delivered through a lick tube via a computer-controlled solenoid valve. See Methods and Supplementary Fig. 1 for details.

(B) The virtual linear track. Screenshots (without the fisheye perspective, see Methods) from the right and left ends of the track are shown. The track (180 cm × 9 cm) was divided into three regions with different textures on the proximal walls (black dots, vertical stripes, white dots). Distal walls (horizontal stripes, green with black crosses) were present at the boundaries between regions. Water rewards were given at the ends of the track, with available rewards alternating between reward sites.

(C) Example trajectories for an individual mouse on training sessions 4 and 10. Position is the animal's location along the track's long axis. Blue dots indicate rewards.

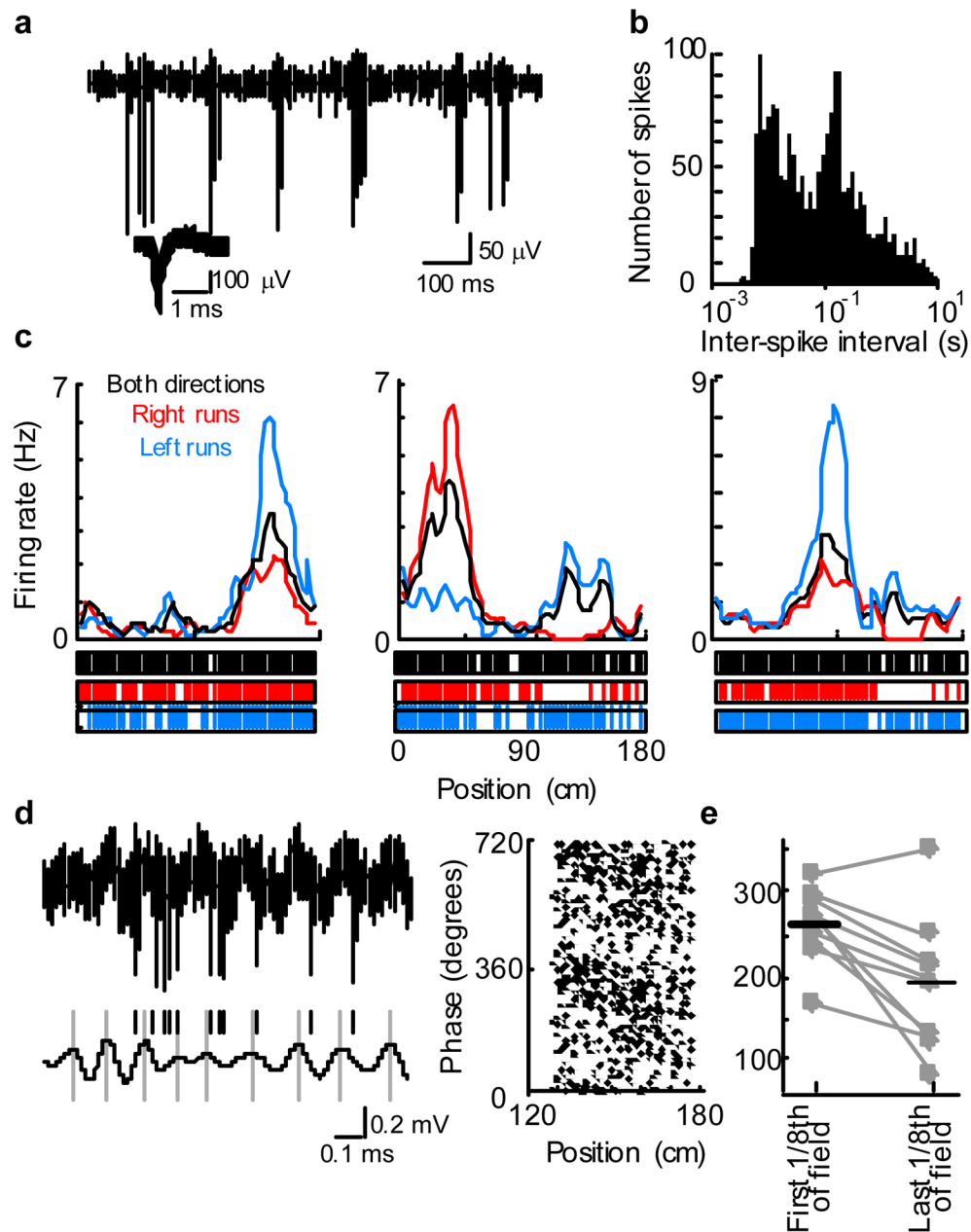(D) Rate of rewards for individual mice (gray lines). The black line indicates the mean. n = 7 mice.

(E) Average distance traveled by the mouse between consecutive rewards. Gray lines indicate individual mice, and the black line is the mean. n = 7 mice.

Figure 3. Extracellular recordings of CA1 place cells along the virtual linear track

(A) An example extracellular recording filtered between 500 Hz and 7.5 kHz. The inset shows overlaid spike waveforms from the recording.

(B) ISI distribution for the full duration of the recording shown in (A). The time axis is plotted on a log scale.

(C) Example firing rate maps for 3 place cells from 3 different mice. Top, Firing rates at positions along the track are shown for rightward runs (red), leftward runs (blue), and runs in either direction (black). Bottom, The position on the track of each spike in the recording is shown as a vertical line. A total of 23 place cells from 8 mice were recorded.

(D) Phase precession of spike times relative to LFP theta. Top left, An example extracellular recording, filtered between 2 Hz and 10 kHz, during a run through the place field. Spikes and the LFP were recorded on the same electrode. Bottom left, The extracellular recording band-pass filtered between 6–10 Hz. Gray lines indicate peaks (0 degrees) in the filtered trace, and black lines indicate the times of spikes. Right, An example plot of phase (two cycles) vs. position on the virtual track for all spikes during complete runs through the place field for a single cell.

(E) Phase values for spikes in the first eighth and last eighth of the place field. Connected points represent a single place field. Horizontal lines indicate the means. n = 10 place fields from 8 cells and 3 mice (multiple place fields are due to the directionality of firing rates).
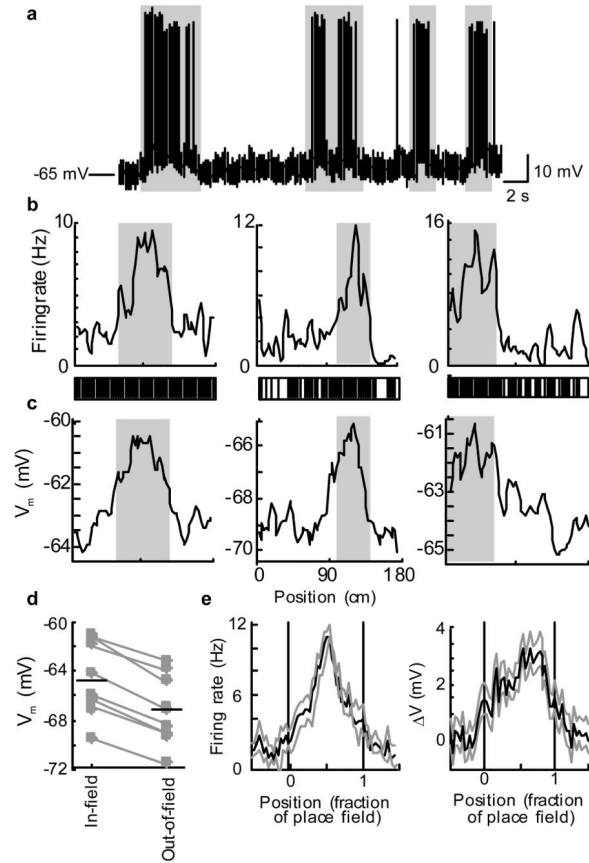
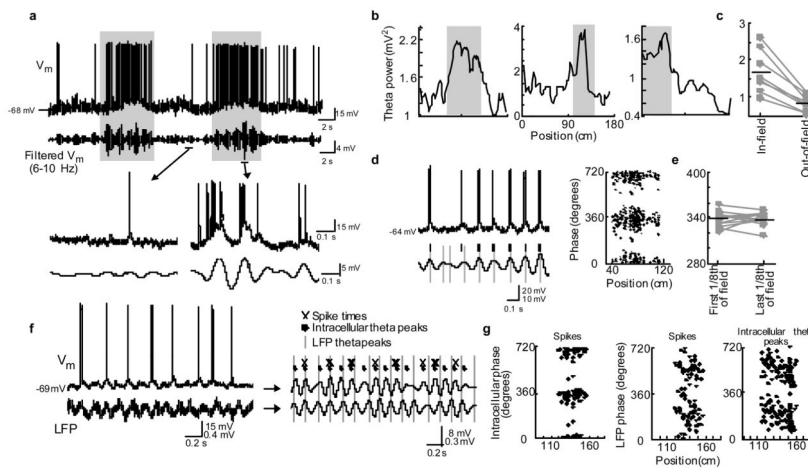**Figure 4. Ramp-like membrane potential depolarization inside place fields**

(A) Example whole cell recording during runs through the cell's place field. Gray boxes indicate the place field (middle example from (B)).

(B) Firing rates along the virtual linear track for 3 place cells recorded intracellularly from 3 different animals. The gray boxes indicate the primary place field determined by firing rates (Methods). Bottom, vertical lines mark the location along the track of every action potential in the recording.

(C) Average baseline membrane potential, excluding action potentials, sorted by position along the track for the three place cells from (B).

(D) Average membrane potential inside and outside the place field. Each pair of connected points is from a single cell. Horizontal lines indicate the means. n = 8 cells from 8 mice.

(E) Average firing rates and changes in baseline membrane potential during complete runs through the place field. To combine data from multiple cells, position values in the place field were normalized. Black lines indicate the mean. Gray lines indicate the mean ± sem. Data are averaged over 84 complete runs through the place field (8 cells).

Figure 5. Membrane potential theta oscillations in place cells

(A) Top, Example whole cell recording during runs through the cell's place field. The band-pass (6–10 Hz) filtered version of the same trace, excluding action potentials, is also shown. Gray boxes indicate the place field (left example from Fig. 4B). Bottom, Expanded portions of the raw and filtered traces taken from the segments at the base of the arrows.

(B) Power in the theta-frequency band sorted by position along the track for the whole cell recordings from Fig. 4. Power was measured as the squared amplitude of the filtered membrane potential trace. Gray boxes indicate the primary place fields.

(C) Theta power inside and outside the place field. Each pair of points represents a single cell. Horizontal bars indicate means. n = 8 cells from 8 mice.

(D) Measurement of spike times relative to intracellular theta. Top left, Example membrane potential trace during a run through the place field. Bottom left, The membrane potential filtered between 6–10 Hz. Gray lines indicate the peaks of theta oscillations (0 degrees). Blacks lines indicate the times of spikes. The vertical scale bar for the unfiltered and filtered trace indicates 20 mV and 10 mV, respectively. Right, Example phase (two cycles) vs. position plot for all spikes during complete runs through a place field for a single cell.

(E) Intracellular phase values for spikes in the first eighth and last eighth of the place field. Each set of connected points indicates a single place field. Black lines indicate the means. n = 12 place fields and 8 cells from 8 mice.

(F) Simultaneous LFP and whole cell recordings. Left, membrane potential and LFP traces during a run through the cell's place field. Right, Filtered (6–10 Hz) membrane potential and LFP traces. The times of LFP theta peaks (gray lines), intracellular theta peaks (circles), and spikes (crosses) are shown to illustrate the phase precession of spikes and intracellular theta relative to LFP theta oscillations and the absence of phase precession of spikes relative to intracellular theta oscillations. Top and bottom scale bar labels correspond to the top and bottom traces, respectively.

(G) Phase precession analysis from a simultaneous LFP and whole cell recording during runs through the place field. Left, Analysis of phase precession of spike times relative to intracellular theta. Middle, Phase precession of spike times relative to LFP theta. Right, Phase precession of intracellular theta peak times relative to LFP theta. Position values are positions on the virtual track.